Electrochimica Acta 552 (2026) 148195

Contents lists available at ScienceDirect

Electrochimica Acta

journal homepage: www.journals.elsevier.com/electrochimica-acta

Ni–Fe-based alloy as oxygen evolving anode for sustainable aluminum production

Kamaljeet Singh [a,b,c,*], Thomas Luke Jamieson [d,e], Gudmundur Gunnarsson [c], Geir Martin Haarberg [b], Isabella Gallino [d,e], Ralf Busch [e], Jon Hjaltalin Magnusson [f], Gudrun Saevarsdottir [a,b]

[a] Department of Engineering, Reykjavik University, 102 Reykjavik, Iceland
[b] Department of Materials Science and Engineering, Norwegian University of Science and Technology (NTNU), 7491 Trondheim, Norway
[c] Taeknisetur IceTec, Arleynir 8, 112 Reykjavik, Iceland
[d] Chair of Metallic Materials, Technical University of Berlin, 10587 Berlin, Germany
[e] Chair of Metallic Materials, Saarland University, 66123 Saarbrücken, Germany
[f] Arctus Aluminium Limited, Arleynir 8, 112 Reykjavik, Iceland

ARTICLE INFO

Keywords:
Inert anode
Aluminum electrolysis
Nickel ferrite
Molten fluoride melts

ABSTRACT

Achieving global net-zero carbon targets by 2050 requires the decarbonization of metal production. Molten salt electrolysis, combined with the rapidly expanding renewable energy sector, provides a transformative and sustainable alternative to conventional metallurgical processes and reduces greenhouse gas emissions. Today, aluminum is produced by electrolysis in molten fluoride melts, using consumable carbon anodes for their feasibility, low cost, good conductivity, and efficient reaction kinetics. However, achieving carbon-free aluminum production requires the development of a cost-effective, non-consumable, and efficient oxygen evolving anode (OEA)—a critical challenge that remains unsolved. Here, we demonstrate an earth-abundant and easily processable Ni–Fe-based anode, capable of forming a protective $NiFe_2O_4$ oxide, both ex-situ and in-situ, that enhances stability and catalytic activity for OEA. The principal approach to evaluating OEA alloy suitability combines analyzing oxide thermodynamics, investigating oxidation kinetics, and performing extended electrolysis in fluoride melts to elucidate the mechanism of protective oxide formation. By optimizing the Ni/Fe ratio in alloy, we demonstrate reduced alloy corrosion, high purity aluminum production, and efficient oxygen evolution. This method lays the framework for a durable and active Ni–Fe-based OEA, thereby advancing carbon-free sustainable aluminum production.

1. Introduction

Shifting toward renewable energy in primary metal synthesis is necessary to curb man-made greenhouse gas (GHG) emissions and to achieve climate goals established in the 2015 Paris Agreement [1,2]. Using molten salt electrolysis, coupled with renewable energy, offers a sustainable path for metal production by slashing GHG emissions and simplifying the process compared to traditional metallurgical methods [2–4]. Established electrochemical processes like the Hall–Héroult for aluminum and molten chloride electrolysis for magnesium demonstrate the viability of this approach. Emerging innovations such as molten oxide electrolysis in steelmaking further push the boundaries of sustainable industrial practices [3,4].

The global demand for primary aluminum reached over 73 million tonnes in 2024, driven by its high recyclability and low density. However, the conventional Hall–Héroult process remains carbon-intensive, producing significant direct GHG emissions—mainly CO_2, CF_4, and C_2F_6—due to the use of a consumable carbon anode (~1.8 tonnes direct CO_2-equivalent per tonne of aluminum) [5]. Despite extensive efforts, a cost-effective, non-consumable, and efficient oxygen evolving anode (OEA) remains unavailable for the aluminum industry in achieving net-zero carbon targets. This limitation is due to severe material degradation under anodic polarization conditions [6–11].

A successful non-consumable OEA in high temperature aluminum production must: (1) resist corrosion at rates below 5 mm·year^{-1}, (2) maintain excellent electrical conductivity, and (3) facilitate oxygen

* Corresponding author.
E-mail addresses: kamaljeet@taeknisetur.is, kamaljeet.singh@ntnu.no (K. Singh).

https://doi.org/10.1016/j.electacta.2026.148195
Received 15 December 2025; Received in revised form 12 January 2026; Accepted 12 January 2026
Available online 13 January 2026

evolution efficiently [6,7,12]. Although precious metals like platinum perform effectively as OEAs in laboratory investigations, developing cost-effective anodes from earth-abundant materials remains essential for achieving commercial viability.

In this context, OEAs made from earth-abundant transition metals, such as Ni–Fe-based alloys, are promising due to their ability to form conductive and protective oxides, enhancing both performance and durability. In recent years, single-phase Ni–Fe–Cu alloys have attracted significant attention for aluminum production in low temperature electrolytes. This is attributed to their stable oxide formation, such as $NiFe_2O_4$, and their enhanced electrocatalytic activity for the oxygen evolution reaction [9–11]. In addition, the anode lifespan can be extended by transitioning from the conventional sodium-based electrolyte (NaF-AlF_3) operating at ~960°C to a new lower temperature potassium–sodium-based electrolyte (KF-NaF-AlF_3) at 800°C, which offers favorable alumina solubility and electrical conductivity [13,14].

For OEAs composed of Ni–Fe–Cu alloys, the Ni/Fe ratio is critical for forming a stable and self-sustaining $NiFe_2O_4$ oxide at 800°C. However, the Cu content must be limited to ~22 wt. % [9,15] to prevent an unstable, corrosion susceptible double-phase region. Additionally, Cu impurities (>0.05 wt. %) from the anode compromise the quality and natural corrosion resistance of primary aluminum. Also, reducing Cu in alloy allows for the economic and direct production of single-phase anodes through casting. On the cathode side, TiB_2 is, so far, the best-known cathode material, offering excellent wettability with liquid aluminum and chemical stability in the fluoride bath [16].

The development of a long-term stable OEA remains a challenge, however, primarily due to the lack of a fundamental understanding of oxide scale growth under anodic polarization in molten fluoride melts. To address this knowledge gap, our study outlines three main objectives. Firstly, developing a reaction scheme and theoretical framework that describes oxide stability in new low temperature electrolytes. Secondly, investigating the high temperature oxidation behavior of a series of Ni–Fe-based alloys, focusing on the relationship between oxidation kinetics, oxide scale structure, and the Ni/Fe ratio. Thirdly, evaluating the alloys' electrolysis performance at an anodic current density (j) of 0.8 $A{\cdot}cm^{-2}$ over a 24 h period by assessing: anode potential stability, oxide scale morphology, aluminum purity, and alloy consumption rate.

As a result, we identified a cost-effective Ni–Fe-based alloy that fulfills the three fundamental requirements of a non-consumable OEA: (1) resisting corrosion at consumption rates below 2 $mm{\cdot}year^{-1}$, (2) forming a conductive $NiFe_2O_4$ oxide scale, and (3) exhibiting effective electrocatalytic activity for oxygen evolution. The protective $NiFe_2O_4$ oxide scale on anode surface was developed in two stages: formed by air oxidation (ex-situ) for short-term stability and sustained by electrochemical oxidation (in-situ) for long-term stability. The structural characteristics of the oxide scale were investigated during both oxidation stages to clarify the mechanisms of oxide scale growth. These findings advance the understanding of the oxidation and corrosion behavior of Ni–Fe-based OEA alloys in molten fluoride melts.

2. Methods

2.1. Anode preparation

Six compositions of the $Ni_{90-x}Fe_xCu_{10}$ alloy series (wt. %), with x ranging from 10 to 60 in increments of 10, were prepared as single-phase (γ-fcc) homogenized alloys and evaluated as OEAs for aluminum electrolysis. High purity metal pieces (purity >99.95 wt. %) of nickel, iron, and copper were weighed and melted under a vacuum-cycled (10^{-3} mbar) argon atmosphere to produce master alloys. These master alloys were subsequently induction melted and cast into 7 mm diameter rods in a water-cooled copper mold under vacuum conditions (MC15 tilt-caster, Indutherm Germany). The rods were then homogenized at 1100°C for 12 h under argon atmosphere to ensure phase consistency. Following this, the homogenized rods were machined into two anode designs: one with a 5 mm diameter and 40 mm length, and another stepped down from 5 mm to 2 mm diameter over 12 mm, with a total length of 40 mm. The surface of the anode was polished with 400-grit SiC abrasive paper, degreased in ethanol, ultrasonically cleaned in distilled water for 15 min, and dried before being used.

To form a protective oxide scale ex-situ on the surface of the anode prior to the electrolysis test, high temperature air oxidation was conducted at 800°C for 8 h in a chamber furnace (300 × 170 × 170 mm, Entech Sweden). The heating and cooling rates were set at $100°C{\cdot}h^{-1}$.

For electrical contact, the anode was connected via a connection rod (diameter 3 × 600 mm, SS316) using a threaded joint. The anode section above the bath, along with the connection rod, was coated with 3 to 5 layers of boron nitride coating (Combat SF, Saint Gobain USA), then shielded within a machined boron nitride shield and an alumina tube shield, respectively. The shield design ensured that any dry corrosion products formed during operation above the melt remained contained within the shields.

2.2. Cathode preparation

A fine grained TiB_2 cathode (purity 99.5 wt. %, Plansee Germany) was used as the counter electrode in this study. Due to its excellent aluminum wettability, the TiB_2 cathode was found to be superior to the typical graphite cathode in the test cell. It suppressed aluminum metal fog formation and prevented the detrimental spontaneous oxide reduction of the anode scale. The cathode was obtained in a rod shape with a diameter of 10 mm and a length of 40 mm. The cathode electrical connection was made by attaching a tight-fitting female graphite connector, secured with platinum wire, enabling a threaded joint with the connection rod. This connection rod was coated with boron nitride and shielded inside an alumina tube.

2.3. Electrolysis experiments

An alumina crucible (OD 65 × depth 140 mm, purity 99.7 wt. %, Meetcera China) containing 300 g of an electrolyte mixture of KF-NaF-AlF_3-Al_2O_3 in a weight ratio of 30.7: 12.4: 53.3: 3.6 was used as the molten fluoride bath. This composition resulted in a CR of 1.3 [(NaF + KF)/(AlF_3)] and a KR of 0.64 [(KF)/(KF + NaF)] in molar ratios. The reagent grade chemicals NaF (purity 99.9 wt. %), KF (purity 99.9 wt. %) and γ-Al_2O_3 (purity 99.5 wt. %) were sourced from Sigma-Aldrich Germany. AlF_3 (99.5 wt. %, Alufluor Sweden) was sublimed in-house at 1100°C under vacuum (10^{-2} mbar), resulting in a final purity of 99.97 wt. %. The chemicals were dried at 300°C for a minimum 48 h, weighed to the required proportions, mixed in a closed lid polypropylene container and transferred to the alumina crucible.

The crucible was then dried for a minimum of 8 h at 500°C under high purity nitrogen atmosphere (purity 99.9999 vol. %) in an externally heated vertical tube furnace (OD 120 × length 700 mm, Entech Sweden), positioned centrally inside the furnace tube. The top and bottom flanges of the furnace tube were water-cooled and fitted inside with alumina radiation shields to ensure a uniform thermal gradient in the crucible, about 4°C. The furnace temperature was ramped up to achieve bath temperature (T) of 800°C and controlled by a Eurotherm 3508 temperature controller. A second crucible of graphite (OD 95 × depth 110 mm, Schunk SE Sweden) was used as a secondary container in case of failure to alumina crucible and to protect the vertical tube furnace.

The reference electrode was liquid aluminum (Al^0/Al^{3+}) inside a closed-end alumina tube (OD 8 mm) featuring a small side opening of 1 mm, located 26 mm above the closed-end, for ionic contact with the molten bath. The reference tube was initially filled with 0.8 g of aluminum (purity 99.998 wt. %) and 0.5 g of electrolyte powder mixture. A tungsten wire (diameter 1 mm, purity 99.95 wt. %) shielded inside an alumina tube (OD 3 mm, purity 99.7 wt. %) with an exposed length of 15 mm was introduced into the reference tube to make

electrical contact with liquid aluminum pool at the bottom. The ohmic drop (iR) between the reference electrode (Al^0/Al^{3+}) and working electrode (anode) was determined by AC impedance spectroscopy, with 85 % compensation applied in all measurements.

To eliminate moisture and trace noble impurities from the molten bath, a pre-electrolysis was conducted with 8 mm diameter high purity graphite electrodes (HTW Germany) at 1.8 V versus Al^0/Al^{3+}. Following this, the anode and cathode were introduced into the furnace and allowed to equilibrate for 10 min above the bath. Then, the anode was lowered under an anodic polarization potential of 2.1 V to prevent direct chemical dissolution reactions in the fluoride bath. These practices were found to be crucial to protect the pre-formed oxide scale and to ensure good performance of anode during electrolysis.

The anode and cathode were positioned vertically and in parallel, 5 cm apart, in the bath with equal immersion depths for uniform current distribution. The geometric areas of the anode and cathode within the bath were used to estimate current densities. The anode areas were 0.53 cm^2 (2 mm diameter rod) and 2.55 cm^2 (5 mm diameter rod), with corresponding cathode areas of 3.30 cm^2 and 5.50 cm^2, which were used to calculate the current density. The alumina crucible served as source of alumina feed during the electrolysis, without any external additions.

Electrochemical measurements, including linear sweep voltammetry (LSV) and constant current electrolysis, were carried out using a software controlled Ivium XP40 potentiostat. For LSV, a 2 mm diameter rod anode was used, whereas a 5 mm diameter rod anode was utilized for constant current electrolysis for durations ranging from 1 to 24 h at j = 0.8 $A{\cdot}cm^{-2}$. Electrolyte samples, ~5 mL, were collected pre- and post-electrolysis using a quartz tube of 5 mm diameter. Upon completing electrolysis, the electrodes were raised from the bath and cooled down inside the furnace with inert atmosphere to retain reaction species.

2.4. Post-electrolysis analysis

The Faradaic current efficiency was determined by the total weight of aluminum extracted from the bottom of the frozen crucible and the weight gain of the TiB_2 cathode after brushing off electrolyte remains. Aluminum collected from the crucible and the cathode was analyzed using ICP-MS to quantify anode constituents, mainly Fe, Ni, and Cu. The electrolyte samples, collected both before and after electrolysis, were analyzed using ICP-OES to determine baseline compositions and to adjust impurity levels in the produced aluminum. The alumina saturation level in the electrolyte was analyzed by oxygen analysis using a LECO instrument.

The surface of anode post-electrolysis was characterized using XRD (PANalytical Empyrean) operating at 40 mA and 45 kV, with a 2θ-scan and step size of 0.013°, using Cu Kα 1.54060 Å. XRD identified phases present on the surface and to a depth of about 10 to 20 μm, based on the penetration depth of the rays and the integrity of the scale. To characterize the microstructural properties of the oxide scale developed on the anode, the cross-section of the anode was prepared. It was cut using a low speed diamond saw and embedded in conductive Bakelite hot-mold resin. The sample was sequentially polished using SiC papers with grit sizes from 220 to 1000, followed by diamond paste ranging from 3 μm to 1 μm. The microstructural and elemental distribution across the anode cross-section were then examined using SEM (Jeol JSM-IT800) coupled with EDS (Oxford Instruments).

2.5. Dry oxidation experiments

Dry oxidation experiments on $Ni_{90-x}Fe_xCu_{10}$ alloy series were conducted using a Thermogravimetric Analyzer (TGA) with a Differential Thermal Analyzer (Netzsch STA 449C Jupiter). Disc samples of alloys, 5 mm in diameter and 3 mm in thickness, were cut from 5 mm alloy rods, produced, homogenized, and finished following the same procedure as specified for anode preparation. High temperature oxidation tests were conducted in a pure $O_{2(g)}$ environment at 1 atm with a flow rate of 50 $mL{\cdot}min^{-1}$. The temperature was set to 800°C at a heating rate of $12°C{\cdot}min^{-1}$ from room temperature. Specific mass gain ($mg{\cdot}cm^{-2}$) was plotted over time (h). Subsequently, the surface and cross section of oxidized samples were characterized using XRD, SEM, and EDS, following the same procedures outlined for anodes post-electrolysis.

3. Results and discussion

3.1. Thermodynamic analysis of oxide stability

First, we analyzed the stability of the oxides formed by the alloy constituents—Ni, Fe, and Cu—in the new KF-NaF-AlF_3-Al_2O_3 electrolyte at 800°C, and we determined the correlation between their oxide dissociation potentials and the activity of alumina. To estimate the oxide dissociation potentials, we applied a formal reaction scheme to identify the possible reactions. Fig. 1 illustrates a formal reaction scheme within the reaction zone of an aluminum electrolysis cell, adapted from the conventional Hall–Héroult cell with modifications to incorporate a vertical electrode configuration and a new KF-NaF-AlF_3-Al_2O_3 based electrolyte [16,17]. In this scheme, Na^+ and K^+ ions facilitate charge transport by migration (M), while aluminum is discharged at the cathode by diffusion (D) of AlF_3 species (such as AlF_4^- and AlF_6^{3-}). Simultaneously, NaF and KF diffuse in the opposite direction to maintain ionic balance. Meanwhile at the anode, alumina (complex Al-O-F species) undergoes electrochemical oxidation, evolving $O_{2(g)}$.

The reaction scheme can be represented as follows:

$$\text{At anode,} \frac{1}{2}Al_2O_{3(diss.)} + 3NaF_{(l)} = \frac{3}{4}O_{2(g)} + AlF_{3(diss.)} + 3Na^+ + 3e^- \quad (1)$$

$$\text{At cathode,} AlF_{3(diss.)} + 3Na^+ + 3e^- = Al_{(l)} + 3NaF_{(l)} \quad (2)$$

$$\text{Cell reaction,} \frac{1}{2}Al_2O_{3(diss.)} = Al_{(l)} + \frac{3}{4}O_{2(g)} \quad (3)$$

The reversible potential for Eq. (3) was calculated using Nernst relation:

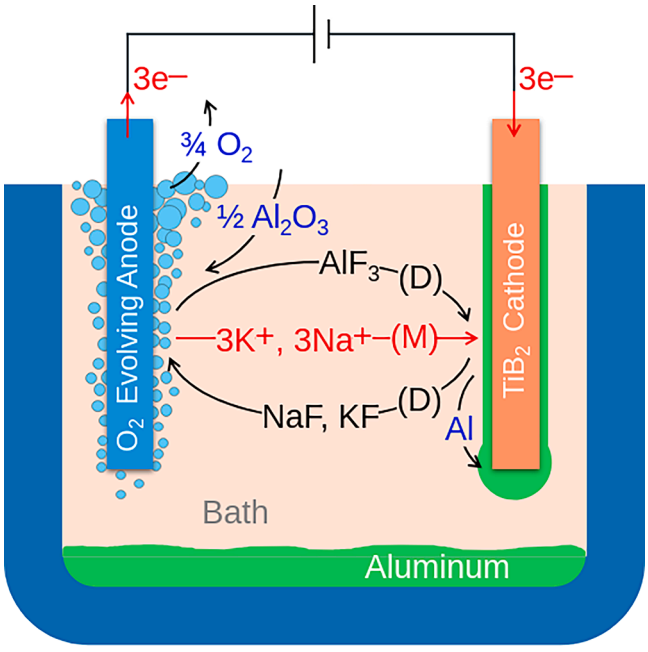

Fig. 1. Schematic illustration of formal reaction scheme in an aluminum electrolysis cell with vertical electrodes, featuring an OEA paired with a wettable aluminum cathode of TiB_2 in a molten bath composed of KF-NaF-AlF_3-Al_2O_3 at 800°C.

$$E_3^{rev} = -\frac{\Delta G_3^0}{zF} - \frac{RT}{zF}\ln\left(\frac{1}{a_{Al_2O_3}^{1/2}}\right) \quad (4)$$

where ΔG^0 is the standard Gibbs free energy (kJ·mol^{-1}), z is the number of exchanged electrons, F is Faraday's constant (96500 C·mol^{-1}), R is the ideal gas constant (8.314 J·K^{-1}·mol^{-1}), T is the temperature (1073 K) and a is the activity of the species involved in the reaction. The activity of all species, except $a_{Al_2O_3}$ and a_{AlF_3}, was considered to be unity. In a melt under alumina saturated conditions, the activity of alumina is expected to be one ($a_{Al_2O_3} \approx 1$).

Using the Ni-Fe-Cu alloy anode—protected by an oxide scale formed either ex-situ or in-situ—the main anodic reaction will involve the evolution of $O_{2(g)}$ from alumina dissolved in the electrolyte. This reaction proceeds in one of two ways: if the oxide (represented as MO_x) of the protective scale is stable and has a higher dissociation potential than the anode potential (E_3^{rev}), then the $O_{2(g)}$ will evolve without consuming the alloy. Conversely, if this MO_x is not stable, the anode alloy will be consumed over time [18]. The dissociation reaction scheme of MO_x and the corresponding reversible dissociation potential are calculated as follows:

$$MO_{x(s)} + yNaF_{(l)} = MF_{y(s)} + \frac{x}{2}O_{2(g)} + yNa^+ + ye^- \quad (5)$$

$$\frac{y}{3}AlF_{3(diss.)} + yNa^+ + ye^- = \frac{y}{3}Al_{(l)} + yNaF_{(l)} \quad (6)$$

where M represents Ni, Fe, and Cu.

Combining Eqs. (5) and (6) gives an overall metal oxide dissociation reaction Eq. (7).

$$\frac{3}{y}MO_{x(s)} + AlF_{3(diss.)} = Al_{(l)} + \frac{3x}{2}O_{2(g)} + \frac{3}{y}MF_{(s)} \quad (7)$$

The reversible dissociation potential of Eq. (7) is:

$$E_7^{rev} = -\frac{\Delta G_7^0}{zF} - \frac{RT}{zF}\ln\left(\frac{1}{a_{AlF_3}}\right) \quad (8)$$

Eq. (8) shows that the magnitude of the dissociation potential (E_7^{rev}) of the oxide (MO_x) decreases as the activity of aluminum fluoride (a_{AlF_3}) increases.

Similarly, for metal aluminates (MAl_2O_4), which readily form from their corresponding oxides and/ or fluorides under anodic polarization, the reaction scheme and dissociation potential are expressed as:

$$MAl_2O_{4(s)} + yNaF_{(l)} = MF_{y(s)} + \frac{1}{2}O_{2(g)} + Al_2O_{3(diss.)} + yNa^+ + ye^- \quad (9)$$

Combining Eqs. (6) and (9) gives the overall metal aluminate dissociation reaction Eq. (10) and corresponding reversible potential in Eq. (11).

$$\frac{3}{y}MAl_2O_{4(s)} + AlF_{3(l)} = Al_{(l)} + \frac{3}{2y}O_{2(g)} + \frac{3}{y}Al_2O_{3(diss.)} + \frac{3}{y}MF_{y(s)} \quad (10)$$

$$E_{10}^{rev} = -\frac{\Delta G_{10}^0}{zF} - \frac{RT}{zF}\ln\left(\frac{a_{Al_2O_3}^{3y}}{a_{AlF_3}}\right) \quad (11)$$

Eq. (11) indicates that the magnitude of the dissociation potential (E_{10}^{rev}) of the aluminate decreases with either an increase in the activity of aluminum fluoride (a_{AlF_3}) or a decrease in the activity of alumina ($a_{Al_2O_3}$).

Using Eq. (4), (8), and (11), the reversible potential of the primary cell reaction $Al_2O_{3(diss.)}/O_{2(g)}$, the dissociation potential of various stable metal oxides (NiO, Fe_2O_3, CuO) and aluminates ($NiAl_2O_4$, $CuAl_2O_4$) of alloy constituents (Ni, Fe, and Cu) were calculated. The HSE Chemistry software was used to compute the ΔG^0 of each reaction [19]. Since the activity data of a_{AlF_3} in the new KF-NaF-AlF_3 system are unavailable in the literature, it was calculated based on the relationship provided for conventional NaF-AlF_3 electrolytes, with NaF/AlF_3 molar ratio 1.3 at a bath temperature of 800°C [16,20]. It is important to note that $NiFe_2O_4$, which is not included in the reaction scheme, is unlikely to convert to corresponding fluorides under the described conditions. This is because NiO, in the presence of the Fe_2O_3, spontaneously forms $NiFe_2O_4$, a thermodynamically stable oxide (ΔG at 800°C= −22.89 kJ·mol^{-1}) [19] with low solubility in cryolite melts [21].

Fig. 2 presents the dissociation potentials of metal oxides and metal aluminates as a function of alumina activity. We can observe two trends. First, the reversible potential of the primary reaction, $Al_2O_{3(diss.)}/O_{2(g)}$, increases as the activity of alumina decreases. Second, as the alumina activity decreases, the gap between the reversible potential of primary reaction and the dissociation potentials of the corresponding oxides and aluminates becomes smaller. In general, if the anode potential exceeds the dissociation potential, all anode oxides/aluminates will ultimately convert to their corresponding stable fluorides, leading to anode consumption or corrosion.

According to Fig. 2, NiO is only stable at low activity of alumina whereas $NiAl_2O_4$ phase is stable at higher activity of alumina. Fe_2O_3 is moderately stable across the entire alumina activity range and is unlikely to convert to a less stable $FeAl_2O_4$ aluminate phase than $FeF_{3(g)}$. The dissociation potential of CuO is highest among all. CuO could form $CuAl_2O_4$ at very high activity of alumina, although this is uncertain because thermodynamic data of $CuAl_2O_4$ in cryolite melts is not well established [22].

Furthermore, this model indicates that the potential difference between $O_{2(g)}$ evolution and oxide dissociation increases with increasing alumina activity, with Cu-based anode showing the largest difference. Consequently, a Cu-based anode would perform optimally for two reasons—the thermodynamic stability and the conductive nature of the Cu-oxide scale. In the literature, various studies on Cu-based anodes have been reported in low temperature electrolytes [23,24]. During electrolysis at 700°C, high Cu content in the alloy, varying from 70 to 85 wt. %, resulted in stable cell voltages due to the formation of a thick oxide scale of CuO [23,24]. This stability behavior is accurately described by the proposed theoretical model. Notably CuO has high solubility in

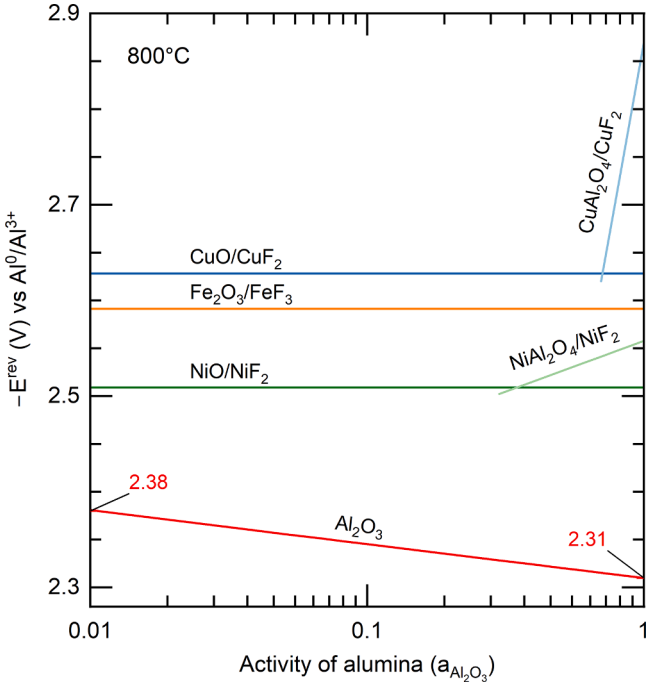

Fig. 2. Thermodynamic analysis of oxide stability of Ni, Fe, and Cu systems, showing reversible potential (E^{rev}) of Al_2O_3, NiO, $NiAl_2O_4$, Fe_2O_3, CuO and $CuAl_2O_4$ as a function of activity of alumina ($a_{Al_2O_3}$) at 800°C. For a saturated alumina bath, $a_{Al_2O_3} \approx 1$.

cryolite [22], resulting in Cu impurities in aluminum beyond a few ppm, which are intolerable due to their harmful impact on its natural corrosion resistance. Similarly, Fe-based anode forms Fe_2O_3, which also has high solubility in cryolite. This results in significant Fe contamination, making them unsuitable [22,25]. In high alumina activity baths, Ni-based anodes tend to form $NiAl_2O_4$, an insulating phase that increases the potential of anode significantly. Studies have shown that Ni-based anodes suffer from severe corrosion due to aluminate and fluoride formation, leading to unstable cell voltages, which is consistent with this model prediction [24,26].

Therefore, the thermodynamic analysis helps in identifying alloying elements that can form stable oxides as a function of activity of alumina ($a_{Al_2O_3}$) and aluminum fluoride (a_{AlF_3}) in low temperature electrolytes. Although Cu- and Fe-based anodes can form stable phases with relatively high dissociation potential, they lead to intolerable metal contamination. In contrast, Ni-based anodes have the lowest dissociation potential and are prone to aluminates and corrosion. Consequently, the analysis indicates that Ni–Fe-based anodes with low Cu content and an optimized Ni/Fe ratio, which promote the formation of stable $NiFe_2O_4$ by consuming less stable NiO and Fe_2O_3, present a promising alternative. However, systematic studies on the optimal Ni/Fe ratio in Ni–Fe-based alloys in low temperature electrolytes remain limited, an area further investigated in this report.

3.2. Oxidation kinetics of $Ni_{90-x}Fe_xCu_{10}$ alloys

$Ni_{90-x}Fe_xCu_{10}$ alloys series were evaluated for OEA in aluminum production and showed remarkable corrosion resistance in aggressive molten fluoride melts. Therefore, understanding the oxidation kinetics of these alloys is of interest. Oxidation experiments were first conducted in a pure oxygen environment at 1 atm and 800°C for 18 h, conditions similar to those encountered by OEA.

The oxidation behavior of Ni–Fe–Cu alloys is controlled by both thermodynamic and kinetic factors governing the formation of complex multilayered oxides. In Ni–Fe–Cu alloy, CuO is thermodynamically stable only at higher partial pressures of oxygen (~10^{-3} atm) near oxide/$O_{2(g)}$ interface, followed by Fe_2O_3 and NiO (Supplementary Fig. s2). However, Fe_3O_4 and FeO are unlikely to form unless the partial pressure of oxygen drops significantly below 10^{-18} atm, which could occur when the oxide scale becomes sufficiently thick (Supplementary Fig. s2) [19]. Among the constituent elements, Cu is the fastest outward diffusing element in Ni–Fe–Cu system followed by Fe and Ni at 800°C which means that CuO is essentially the outermost oxide favored by both thermodynamics and kinetics [27,28]. Beneath the CuO, Fe_2O_3 and NiO spontaneously react to produce the protective $NiFe_2O_4$ oxide spinel—a characteristic feature of the Ni–Fe–Cu alloy for OEA application [11].

However, the formation of a multilayered oxide scale may influence the rate of ion transport and oxidation kinetics, depending on the defect structures within each oxide. Therefore, the defect structures of the oxides in the scale, such as $NiFe_2O_4$ and NiO, play an important role. $NiFe_2O_4$ oxide is characterized by an inverse spinel structure where Ni^{2+} cations occupy half of the octahedral site and rest half and whole tetrahedral sites by Fe^{3+} cations [29]. The Fe diffusion through $NiFe_2O_4$ is faster than Ni as the activation energy required for the former is 1 eV compared to 1.4 eV for the latter [29]. In contrast, for NiO—a Mott–Hubbard insulator with a band gap of ~4.3 eV—significantly slows Ni diffusion, with activation energies reaching up to 11.86 eV [30]. This suggests that the $NiFe_2O_4$ layer promotes efficient ion transport, whereas the NiO layer may hinder it, resulting in limited growth of the protective oxide scale on Ni–Fe-based alloys. Therefore, optimizing the Ni/Fe ratio to favor the formation and growth of desired oxide phases offers an effective approach to regulating ion transport and oxidation kinetics in the alloy.

Previous high temperature oxidation studies of Ni–Fe–Cu alloys in pure oxygen at 700–850°C using TGA have confirmed a parabolic oxidation behavior, characteristic of a diffusion-controlled mechanism with slow kinetics [9,23,28,31]. The oxidation kinetics of Ni–Fe–Cu alloys were found to be highly sensitive to both the oxidation temperature and the Cu content of the alloy. The kinetics slow down significantly with decreasing temperature (below 850°C, where the behavior changes from linear to parabolic) and with decreasing Cu content (as Cu is the fastest diffusing element in the system) [9,23,28]. This presents an opportunity: at a sufficiently low oxidation temperature of 800°C (to remain within the parabolic kinetic regime), with Cu content as low as 10 wt. % in the selected $Ni_{90-x}Fe_xCu_{10}$ alloys series, a thermodynamically stable and kinetically protective oxide scale may form. The following section presents the results on the high temperature oxidation behavior of the $Ni_{90-x}Fe_xCu_{10}$ alloys series in pure oxygen at 800°C.

Fig. 3 a shows the TGA curves and oxidation kinetics of each alloy. The sharp peak in the oxidation curve of $Ni_{80}Fe_{10}Cu_{10}$ and $Ni_{70}Fe_{20}Cu_{10}$ alloys within the first 5 h indicates localized cracking (Fig. 3 a, inset). Subsequently, the curve returns to normal, indicating the formation of a more adherent and stable oxide scale. No evidence of catastrophic breakaway oxidation or flaking of the oxide was observed in any of the experiments. TGA curves can be described by the power law behavior according to Eq. (12).

$$(\Delta M)^m = k_m \Delta t + C \tag{12}$$

where k_m is the rate constant ($g^2 \cdot cm^{-4} \cdot s^{-1}$), ΔM the specific mass gain ($mg \cdot cm^{-2}$), Δt the time (s), and C the integration constant. An increase in the exponent 'm' corresponds to a slower oxidation rate.

The oxidation kinetics of $Ni_{90-x}Fe_xCu_{10}$ alloys series were found to be complex, which in most cases could be effectively approximated by the parabolic rate law. Accordingly, fitting the TGA curves in Fig. 3 a for the steady-state region (after 5 h) revealed an approximate parabolic behavior (m = 2) for each alloy, although the oxidation rate of $Ni_{30}Fe_{60}Cu_{10}$ alloy shows a significant deviation. After about 7 h, the $Ni_{30}Fe_{60}Cu_{10}$ alloy transitions from a parabolic to a stable cubic regime (m = 3), indicative of a slower growth regime despite possessing lower Ni (highest Fe) content. This behavior is likely explained by the rapid oxidation of the alloy during the first 7 h, which forms a sufficiently thick and adherent scale that significantly inhibits the inward diffusion of oxygen. Therefore, a similar evolution toward a cubic regime may yet be observed at longer oxidation run times for alloys containing 40–80 wt. % Ni. The oxidation rate constant in Table 1 obtained for these alloys is consistent with reported literature values [9,23,28,31,32].

Notably, in Fig. 3 b, the mass gained at 800°C oxidation in pure oxygen oxidation (18 h), compared to air oxidation (8 h), is not significantly higher, despite the longer exposure time (Supplementary Fig. s3). This aligns with the literature, indicating that the oxidation of Ni–Fe–Cu alloys is largely influenced by temperature rather than by oxygen partial pressure [9,23,28].

The oxide scale typically exhibits a stratified structure composed of four primary layers, as previously reported [11]. As illustrated in Fig. 4, moving from the outer oxide/$O_{2(g)}$ interface towards the alloy, these layers comprise, in sequence, CuO, Fe_2O_3, $NiFe_2O_4$, NiO, along with minor mixed oxides.

Interestingly, two distinct oxide scale morphologies were observed based on the Ni content in the alloy, as revealed by SEM-EDS elemental analysis (Fig. 4) and XRD phase analysis (Fig. 5). Alloys with high Ni content 70–80 wt. % developed a Ni-rich oxide scale, predominantly composed of NiO, whereas alloys with lower Ni content 30–40 wt. % developed an Fe-rich oxide scale, primarily containing $NiFe_2O_4$ and Fe_2O_3. For intermediate compositions with Ni content 50–60 wt. % alloys, a mixed morphology was noted, indicating a compositional transition from Fe-rich to Ni-rich scales with increasing Ni content.

At the macroscopic level, the two oxide scale types—Ni-rich and Fe-rich—exhibited distinctly different morphologies. The Ni-rich scale (Fig. 4 a, b) displayed porosity, poor adhesion to the base alloy, and notable defects. In contrast, the Fe-rich scales (Fig. 4 c) were dense, well-adherent, and demonstrated superior structural integrity.

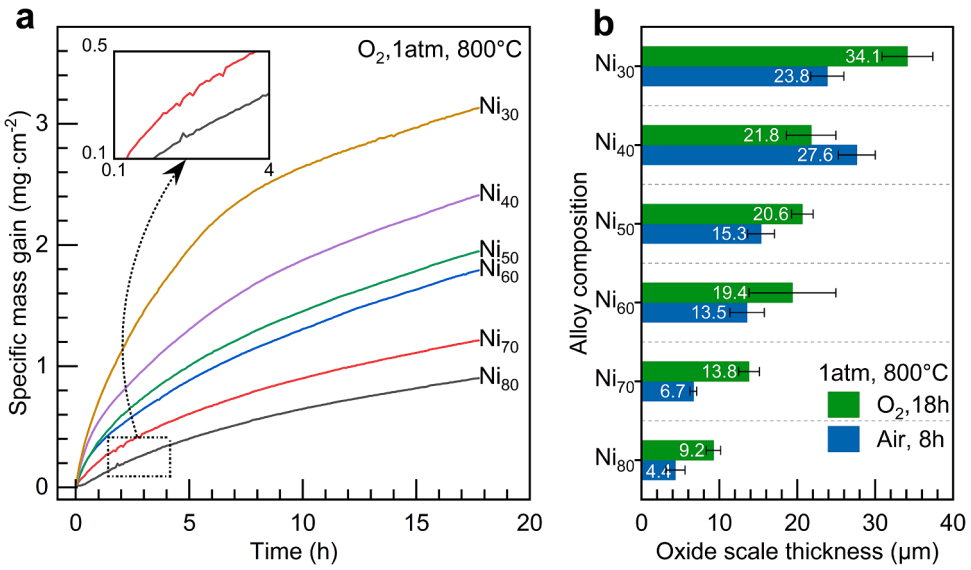

Fig. 3. TGA oxidation kinetics of $Ni_{90-x}Fe_xCu_{10}$ alloys series. (a) Specific mass gain for each alloy composition, denoted simply as Ni_{90-x}, measured in 1 atm of $O_{2(g)}$ at 800°C for 18 h duration; the inset graph shows an enlarged view of the highlighted area. (b) Oxide scale thickness formed after oxidation at 800°C, comparing results from 18 h in $O_{2(g)}$ and 8 h in air, with thicknesses quantified from cross-sectional measurements via SEM (std. dev., n = 5 measurements).

Table 1
Summary of TGA oxidation data derived from Fig. 3 a, presenting the oxidation rate constants for the $Ni_{90-x}Fe_xCu_{10}$ alloys series, obtained under conditions of 1 atm $O_{2(g)}$ at 800°C for 18 h.

Alloy composition	Parabolic rate constant, k_p	Cubic rate constant, k_c
(wt. %)	($g^2 \cdot cm^{-4} \cdot s^{-1}$)	($g^3 \cdot cm^{-6} \cdot s^{-1}$)
$Ni_{80}Fe_{10}Cu_{10}$	1.60×10^{-12}	
$Ni_{70}Fe_{20}Cu_{10}$	1.45×10^{-11}	
$Ni_{60}Fe_{30}Cu_{10}$	1.72×10^{-11}	
$Ni_{50}Fe_{40}Cu_{10}$	4.73×10^{-11}	
$Ni_{40}Fe_{50}Cu_{10}$	3.70×10^{-10}	
$Ni_{30}Fe_{60}Cu_{10}$		2.59×10^{-17}

The Ni-rich scales, where NiO formed the predominant oxide phase, were associated with slower oxidation kinetics. This behavior was evidenced by thin scale development (Fig. 3 b), a low parabolic rate constant (Table 1), and minimal mass gain (Supplementary Fig. s3). Together, these features suggest that the NiO layer acts as an effective diffusion barrier, restricting both the outward diffusion of metallic cations and the inward diffusion of oxygen anions [33]. This interpretation is further supported by the absence of a depletion region in Fig. 4 a, which limits the oxide scale thickness of the Ni_{70} and Ni_{80} alloys to less than 14 μm (Fig. 3 b).

For intermediate alloy compositions containing Ni 50–60 wt. %, a thin, continuous NiO layer (~3 μm) remains present at oxide/alloy interface, with an overall scale thickness of about 20 μm (Fig. 3 b). However, when the Ni content drops below 50 wt. %, the oxide composition shifted toward an Fe-rich scales, with $NiFe_2O_4$ and Fe_2O_3 as the primary constituents. In these alloys, a distinct depletion region emerged, characterized by the absence of a continuous NiO layer [32]. Instead, a non-stoichiometric form of $Ni_xFe_{3-x}O_4$ spinel rich in Fe, was formed at the oxide/alloy interface, potentially representing a solid solution of NiO and Fe_3O_4—a thermodynamically favored phase as scale thickens (Supplementary Fig. s2). The thickness of oxide scales in the Ni_{30} and Ni_{40} alloys ranged from 22 to 34 μm (Fig. 3 b).

Overall, the oxidation rate of the $Ni_{90-x}Fe_xCu_{10}$ alloys series (with low Cu content) at 800°C was found to be reasonably slow, following a parabolic trend. Notably, as Ni content decreased, especially in the $Ni_{30}Fe_{60}Cu_{10}$ alloy, the oxidation kinetics transitioned from a parabolic to a slower cubic regime. Because alloys with Ni 30–40 wt. % lack a continuous NiO layer, they develop dense, well-adherent Fe-rich scales that exhibit superior structural integrity—an essential attribute for protective oxide formation in OEA applications.

3.3. *Electrolysis performance of $Ni_{90-x}Fe_xCu_{10}$ anode*

A series of $Ni_{90-x}Fe_xCu_{10}$ alloys, building on prior successful trials, has been tested for OEA in aluminum electrolysis [10,11,34]. We selected anode alloys containing a fixed 10 wt. % Cu and varying Ni contents (30–80 wt. %) to ensure the development of a stable, protective oxide scale with slow oxidation kinetics and to maintain a corrosion resistant single-phase (γ-fcc) alloy structure during electrolysis at 800°C. These alloys had demonstrated remarkable performance in earlier trials [11]. A low temperature KF-NaF-AlF_3-based electrolyte at 800°C was chosen due to its better alumina solubility, reasonable electrical conductivity, and stable liquidus plateau [13,14], which provides optimal compatibility for ledge cell design. Alloy performance during electrolysis was investigated under constant current mode at a fixed anodic current density of 0.8 $A \cdot cm^{-2}$ for durations between 1 and 24 h, revealing the mechanism of protective oxide scale growth.

3.4. *$Ni_{40}Fe_{50}Cu_{10}$ anode*

The electrolysis test with $Ni_{40}Fe_{50}Cu_{10}$ anode demonstrated stable operation for 24 h (Fig. 6a). The anode potential remained steady at ~4 V, with no obvious fluctuations, highlighting the alloy's strong electrochemical durability. The catalytic activity and stability of the alloy were further evaluated under similar conditions using LSV (Fig. 6 b). The anodic polarization curve revealed no apparent oxidation current before the onset of $O_{2(g)}$ evolution potential of approximately 2.4 V, and the potential required to reach a current density of 0.8 $A \cdot cm^{-2}$ was about 2.9 V. This increased by only 90 mV after 3 h of electrolysis, indicating high stability in performance. After the 24 h electrolysis test, there was no observable change in the anode's dimensions (Fig. 6 c). Aluminum was produced on the TiB_2 cathode, which was adequately covered with the metal (Fig. 6 d), while additional aluminum that dripped from cathode and collected at the bottom of the crucible was recovered (Fig. 6 e). The total mass of the produced aluminum was used to calculate the Faradaic current efficiency, which reached 90 %, while the purity of metal measured 99.9 wt. % (Fig. 6 f). This level of performance is especially impressive for a system of this scale. Based on the impurities

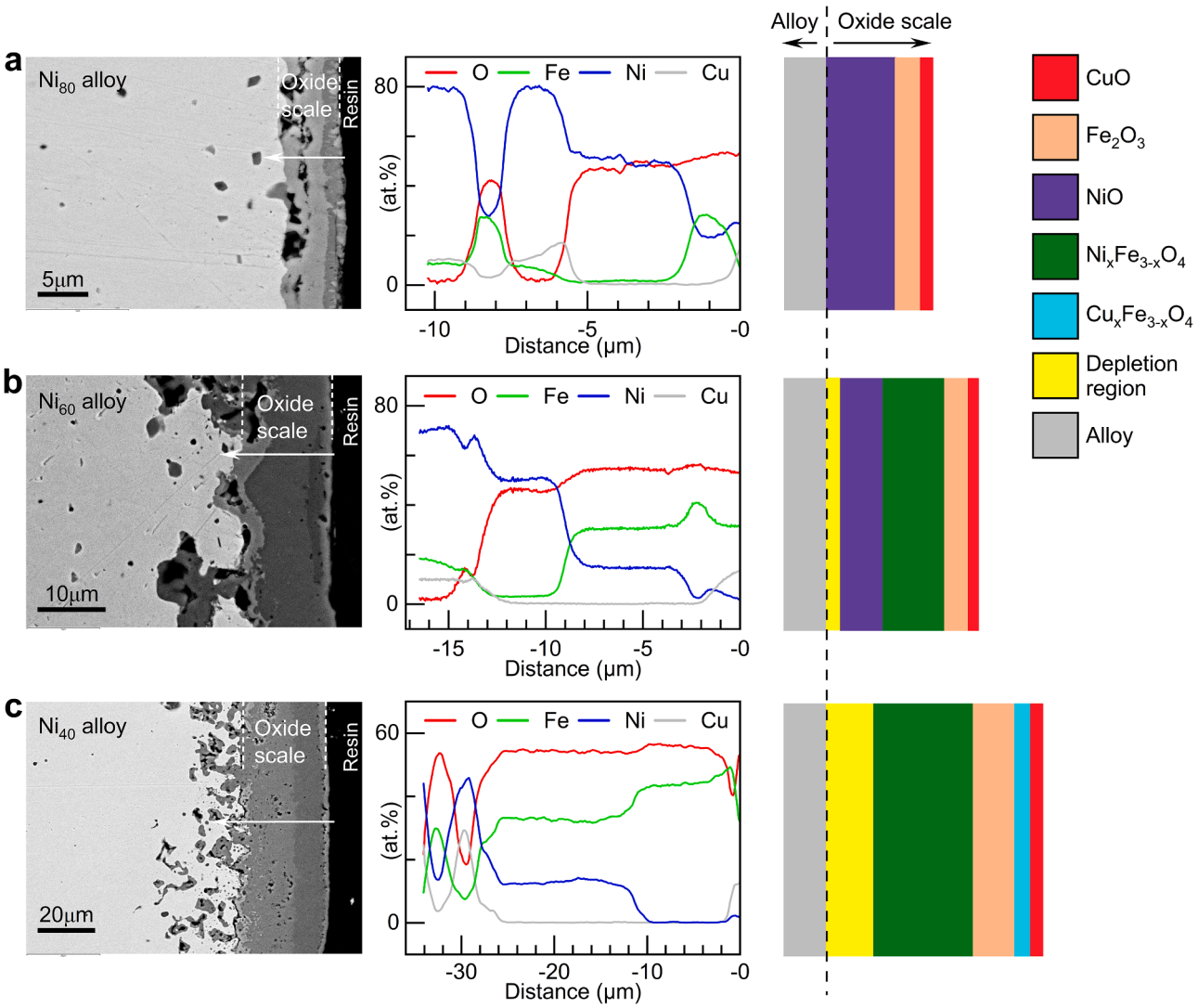

Fig. 4. Cross-sectional analysis revealed multilayered oxide scale formation in the $Ni_{90-x}Fe_xCu_{10}$ alloys series following oxidation treatment in air at 800°C for 8 h, presented as SEM images (left) with corresponding EDS line scans (center) and schematics of oxide layer structures (right) for each alloy composition: (a) $Ni_{80}Fe_{10}Cu_{10}$, (b) $Ni_{60}Fe_{30}Cu_{10}$, and (c) $Ni_{40}Fe_{50}Cu_{10}$.

from the anode (Ni, Fe, and Cu) in the electrolyte and the produced aluminum, the alloy consumption rate was calculated to be 2 mm·year^{-1}—well below the typical limit of 5 mm·year^{-1} for OEA [12].

The stability of the $Ni_{40}Fe_{50}Cu_{10}$ alloy correlates with the formation of a dense and protective $NiFe_2O_4$ oxide layer (Fig. 4 c), which was pre-formed ex-situ by high temperature air oxidation and is likely to remain stable during in-situ electrochemical oxidation. Cross sectional analysis of the oxide scale after electrolysis, however, revealed a complex structure with several notable features (Fig. 7 a). First, an intact and limited growth of the scale, 219 ± 33 μm thick, was detected, with minimal electrolyte penetration confined to localized spots. Second, and of importance to the high performance of the anode, a characteristic dual-layered oxide structure was identified. This dual-layered oxide structure comprised an outer layer of stoichiometric $NiFe_2O_4$ spinel at the oxide/electrolyte interface and an inner layer of non-stoichiometric, Fe-rich $Ni_xFe_{3-x}O_4$ spinel at the oxide/alloy interface. EDS line analysis (Fig. 7 a, points 1–2, and Supplementary Table s1) confirmed that the outer layer (~120 μm thick) possessed a Ni/Fe atomic ratio close to 0.5, consistent with stoichiometric $NiFe_2O_4$ spinel, whereas the inner layer (~90 μm thick) exhibited a lower Ni/Fe ratio of about 0.3 (Fig. 7 c), indicative of a non-stoichiometric, Fe-rich $Ni_xFe_{3-x}O_4$ spinel.

It has been reported that this non-stoichiometric Fe-rich $Ni_xFe_{3-x}O_4$ spinel enhances the conductivity of the scale, attributed to the formation of oxygen vacancies [35]. XRD analysis (Fig. 7 d) confirmed these observations, identifying $NiFe_2O_4$ and Fe_2O_3 as the major constituent of scale, with a noticeable signal from frozen electrolyte. The Fe-rich $Ni_xFe_{3-x}O_4$ spinel at the oxide/alloy interface likely represents a solid solution of NiO and Fe_3O_4, which is thermodynamically stable under the low oxygen activity within the scale (Supplementary Fig. s2), leading to a substantial increase in conductivity [35]. Remarkably, this Fe-rich spinel can readily convert to stoichiometric $NiFe_2O_4$ spinel under higher oxygen partial pressure encountered at the oxide/electrolyte interface, showing the self-regenerating capability of the protective oxide scale. These observations are consistent with the electrochemical performance of the alloy, which maintained high catalytic activity, a stable voltage, and low consumption throughout the 24 h test (Fig. 6). This indicates that the scale growth of $Ni_{40}Fe_{50}Cu_{10}$ alloy remained stable, self-sustaining, and protective under operating conditions.

3.5. $Ni_{80}Fe_{10}Cu_{10}$ anode

In contrast to the low Ni alloys (30–40 wt. %), the high Ni alloy, $Ni_{80}Fe_{10}Cu_{10}$, exhibited severe corrosion throughout the 24 h electrolysis test (Fig. 8), which significantly contaminated the produced

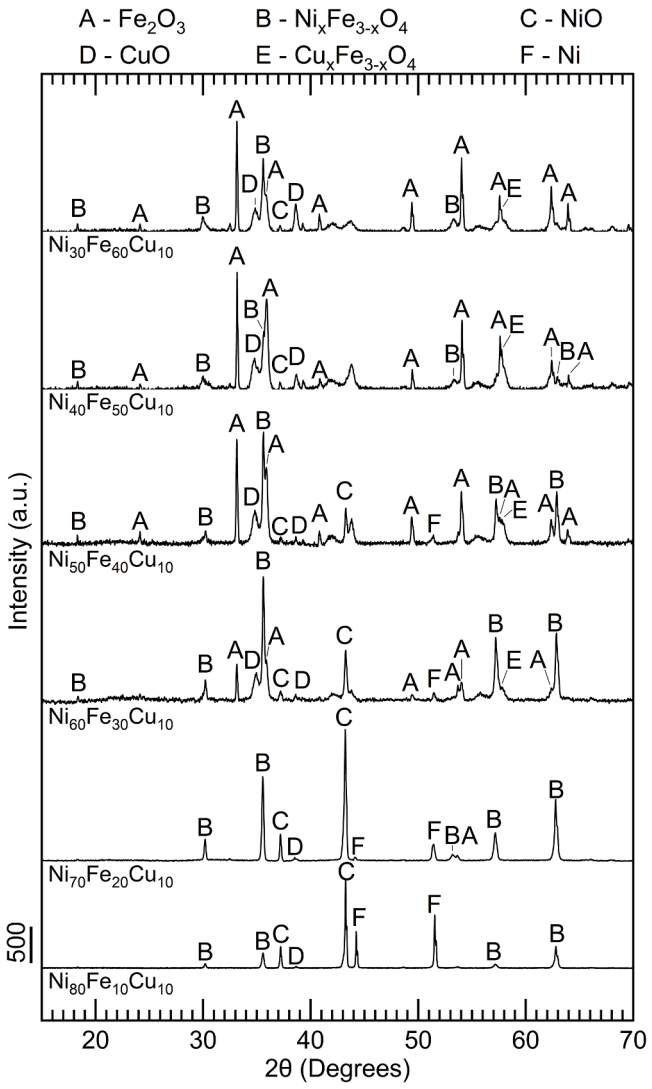

Fig. 5. XRD pattern of the oxide scale surface for $Ni_{90-x}Fe_xCu_{10}$ alloys series after oxidation in air at 800°C for 8 h.

aluminum. The produced aluminum had a purity of only 99.22 wt. % (with anode impurities comprising Ni–0.39 %, Cu–0.25 %, and Fe–0.15 %). The Faradaic current efficiency decreased to 71 % due to elevated anode impurities in the bath, which may undergo cyclic redox reactions and thus lower the current efficiency [16]. As shown in Fig. 8 a, the anode potential quickly rose to the upper limit of 10 V within 2 h and remained above 6 V for the remainder of the test, indicating continued degradation of the alloy.

The oxide scale that developed on the $Ni_{80}Fe_{10}Cu_{10}$ anode proved to be a poor catalyst for $O_{2(g)}$ evolution in the molten fluoride bath. Initially, an anodic current density of 0.8 A·cm^{-2} was achieved at 3.38 V (Fig. 8 b); however, after 3 h, the current density was halved at the same potential, reflecting the insulating nature of the growing oxide scale. This decline in catalytic performance coincided with rapid oxide scale growth during electrolysis, increasing from 4 ± 1.2 μm at 0 h (Fig. 4 a) to 195 ± 34 μm after 1 h (Fig. 8 c), and reaching 394 ± 109 μm after 3 h (Fig. 8 d). Based on these observations, the degradation mechanism of the alloy can be divided into three successive stages of oxide scale growth.

In the first stage, a primary NiO layer—pre-formed by air oxidation—developed on the alloy surface. After 1 h of electrolysis, this layer grew to 195 ± 34 μm (Fig. 8 c) with no significant electrolyte penetration. This indicates that the increase in anode potential (Fig. 8 a) mainly resulted from the increased ohmic resistance caused by NiO scale growth (Fig. 8 c, points 1–3, and Supplementary Table s2). The thermodynamic stability of NiO at low oxygen partial pressures (Supplementary Fig. s2), combined with the limited outward diffusion of Ni in NiO due to its defect structure [30], suggests that scale growth proceeds via internal oxidation at the oxide/alloy interface through the inward diffusion of O^{2-} ions [9,28].

In the second stage (between 1 and 3 h of electrolysis; Fig. 8 d), the oxide scale developed a complex three-layered structure. The outermost layer consisted of a thin (~8 μm) stoichiometric $NiAl_2O_4$ spinel (points 1–2 in Fig. 8 d, and Supplementary Table s3), forming a clear boundary between the molten bath and the underlying scale. Beneath this, a dense middle layer (~350 μm) composed mainly of O, Ni, Al, and Fe was observed (EDS line scan in Fig. 8 e). This middle layer exhibited a relatively high Al concentration (~17.4 at. %) and no detectable Na, K, or F, indicating a chemical gradient of Al from the outer layer. This behavior is consistent with literature that reported selective Al diffusion in the scale of Ni-rich alloys after electrolysis [26]. EDS analysis (Fig. 8 e) further indicated that this middle layer contained a non-stoichiometric spinel, $Ni_xAl_{1-x}O_4$. Next, an innermost layer of NiO (~45 μm) formed adjacent to the alloy substrate (point 4 in Fig. 8 d, and Supplementary Table s3). Consequently, the oxide scale consisted of three sequential layers: an outermost $NiAl_2O_4$ spinel layer, a middle non-stoichiometric $Ni_xAl_{1-x}O_4$ spinel layer, and an innermost NiO layer. This multilayered structure reflects the coupled diffusion-controlled ionic transport and chemical–electrochemically driven oxidation reactions that occur during electrolysis. The formation of $NiAl_2O_4$ can be attributed to the high alumina activity under saturated bath conditions, as confirmed by LECO analysis (data not shown). Under such conditions, NiO becomes unstable and transforms into the thermodynamically favored $NiAl_2O_4$ phase (Fig. 2).

The third stage is marked by excessive growth of the insulating oxide scale, which raised the anode potential beyond the dissociation potential of the oxide. Having a thin aluminate layer on the anode presents a unique condition—it may redistribute the current on the anode surface, causing locally high current density at aluminate-free regions. This high anodic current density breaks down the (protective) oxide scale, exposing the unprotected, oxide-free base alloy to the corrosive fluoride bath. The exposed oxide-free alloy will draw more current at higher anode potential and will undergo severe corrosion [8]. As shown in Fig. 8 a, the anode potential peaked at 10 V after 3 h of electrolysis and oscillated between 6 V and 10 V thereafter, ultimately causing fragmentation and spallation of the oxide scale (Fig. 8 d) and failure of the alloy. XRD analysis confirmed the presence of both NiO and $NiAl_2O_4$ as major phases (Fig. 8 f), consistent with thermodynamic model predictions (Fig. 2). Although NiF_2 layer was not detected in XRD, this might be due to its easy dissolution in the molten bath or poor adhesion under the action of oxygen bubbles.

In summary, the high Ni alloys $Ni_{80}Fe_{10}Cu_{10}$ and $Ni_{60}Fe_{30}Cu_{10}$ (refer to Supplementary Note 1) exhibited rapid oxide growth and a pronounced decline in current density due to the poor catalytic performance of NiO and the formation of insulating $NiAl_2O_4$. Severe anode degradation produced low purity aluminum and increased alloy consumption rates to 16 mm·year^{-1} for $Ni_{80}Fe_{10}Cu_{10}$ and 15 mm·year^{-1} for $Ni_{60}Fe_{30}Cu_{10}$.

3.6. Ni_{70}, Ni_{50}, and Ni_{30} anode

The performance of the $Ni_{70}Fe_{20}Cu_{10}$, $Ni_{50}Fe_{40}Cu_{10}$, and $Ni_{30}Fe_{60}Cu_{10}$ alloy anodes showed a range of behaviors, reflecting the influence of Ni content on stability and catalytic efficiency (Fig. 9). The $Ni_{70}Fe_{20}Cu_{10}$ (Fig. 9 a) and $Ni_{50}Fe_{40}Cu_{10}$ (Fig. 9 b) alloys followed trends similar to those of the $Ni_{80}Fe_{10}Cu_{10}$ (in the previous section) and $Ni_{60}Fe_{30}Cu_{10}$ alloys (refer to Supplementary Note 1), respectively, but with variations in stability duration. Notably, the $Ni_{50}Fe_{40}Cu_{10}$ alloy maintained stable operation for up to 12 h before its potential rose

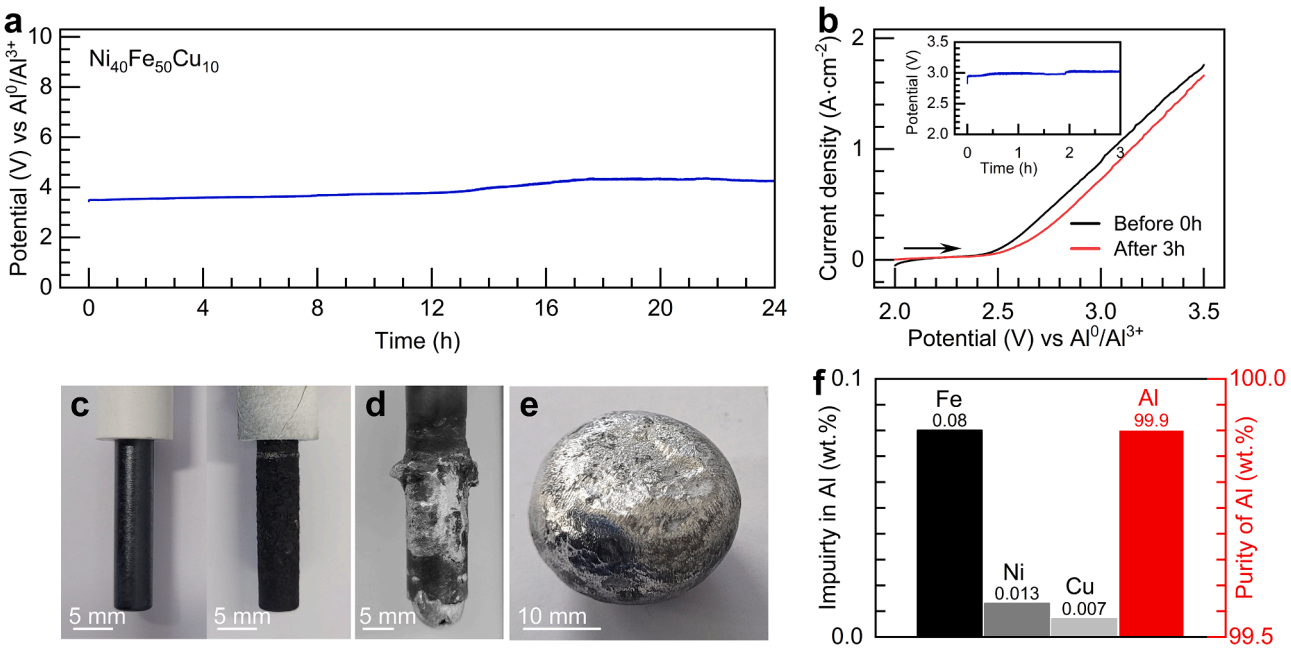

Fig. 6. Performance of $Ni_{40}Fe_{50}Cu_{10}$ alloy anode during electrolysis in molten fluoride bath at 800°C. (a) Evolution of anode potential as a function of electrolysis time. (b) LSV curve at a sweep rate of 100 $mV{\cdot}s^{-1}$; the inset graph shows the evolution of anode potential during 3 h of electrolysis. (c) Image of the $Ni_{40}Fe_{50}Cu_{10}$ alloy anode before (left) and after (right) electrolysis. (d) Image of the TiB_2 cathode after electrolysis, showing deposition of aluminum layer. (e) Extracted aluminum from the bottom of the frozen crucible. (f) Aluminum purity with respect to anode alloy constituents.

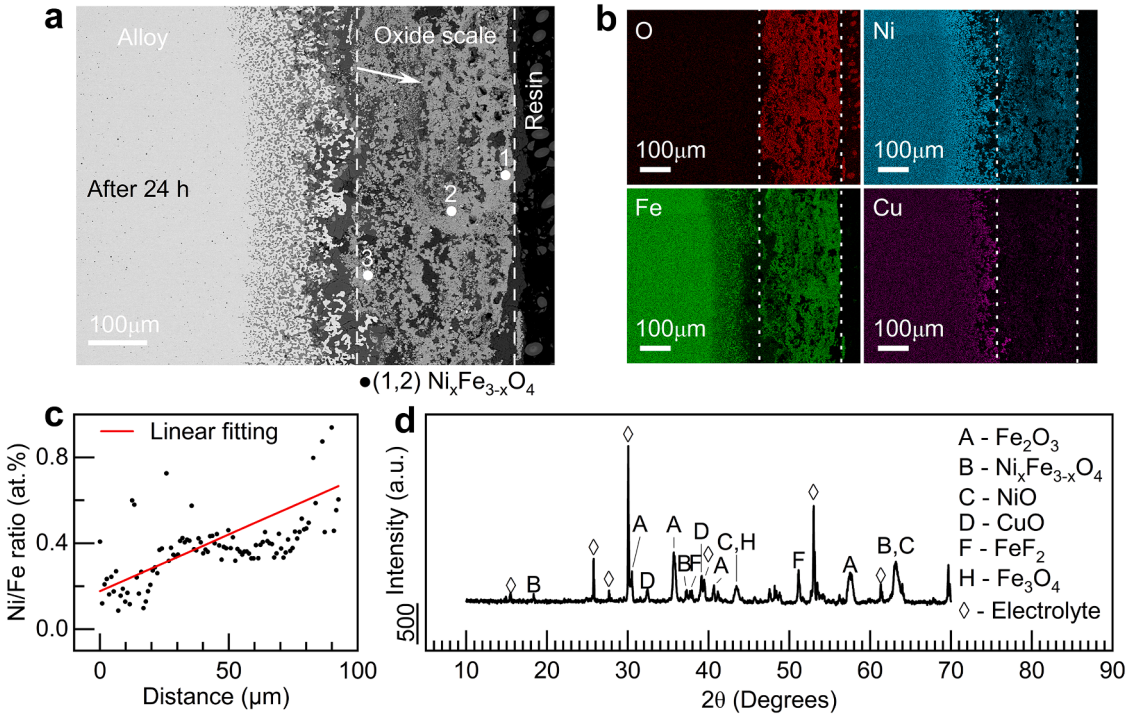

Fig. 7. $Ni_{40}Fe_{50}Cu_{10}$ alloy anode formed a protective $NiFe_2O_4$ oxide during 24 h electrolysis at 800°C. (a) SEM image in backscattered electron (BSE) mode of the anode cross-section. The arrow in the oxide scale at the top right indicates the path for line analysis shown in (c), moving from the oxide/alloy interface toward the outer scale. The number markers 1, 2, and 3 within oxide scale in (a) indicate the point at which EDS point analysis was performed (Supplementary Table s1). (b) EDS mapping of the SEM image for O, Ni, Fe and Cu elements. (c) EDS line analysis of the Ni/Fe atomic ratio along the arrow in (a), revealing an increasing Fe concentration near the oxide/alloy interface. (d) XRD pattern of oxide scale on the anode surface.

sharply to 6 V after 16 h (Fig. 9 b), highlighting the importance of evaluating the performance of OEA over longer durations. In contrast, the high Fe-content alloy, $Ni_{30}Fe_{60}Cu_{10}$ in Fig. 9 c, exhibited the most stable anode potential among all tested alloys in $Ni_{90-x}Fe_xCu_{10}$ series.

A closer examination of anode potential evolution (Fig. 9 a–c) in relation to oxide morphology from SEM (Fig. 9 d), elemental mapping from EDS (Fig. 9 e) and phase analysis from XRD (Fig. 9 f) revealed distinct variations in electrolyte penetration that correlated strongly

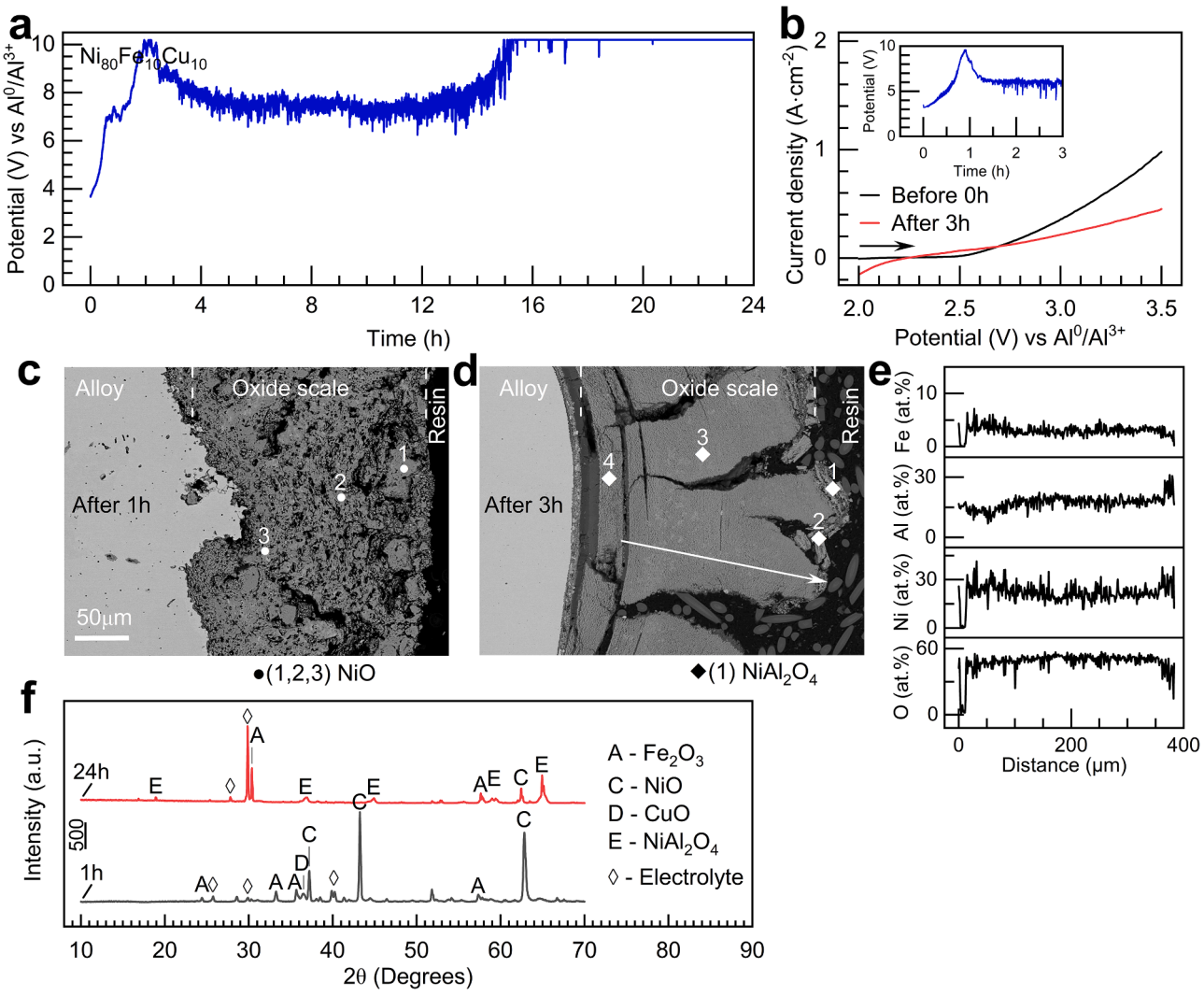

Fig. 8. Performance of $Ni_{80}Fe_{10}Cu_{10}$ alloy anode during electrolysis in molten fluoride bath at 800°C. (a) Evolution of anode potential as a function of electrolysis time. (b) LSV at a sweep rate of 100 mV·s^{-1}; the inset graph shows the evolution of anode potential during 3 h of electrolysis. (c) SEM-BSE image of the anode cross-section after 1 h of electrolysis, and (d) after 3 h of electrolysis, with number markers indicate the point at which EDS point analysis was performed (Supplementary Table s2 and s3). The arrow mark in (d) indicates the path for line analysis shown in (e), moving from the oxide/alloy interface toward the outer scale. (e) EDS line analysis for major elements (O, Ni, Al, and Fe). (f) XRD pattern of oxide scale on the surface of anode after 1 h and 24 h of electrolysis.

with the anode's stability. XRD analysis (Fig. 9 f) confirmed the presence of $NiAl_2O_4$ on the surface the unstable $Ni_{70}Fe_{20}Cu_{10}$ and $Ni_{50}Fe_{40}Cu_{10}$ alloys, while the stable $Ni_{30}Fe_{60}Cu_{10}$ alloy developed a scale mainly composed of Fe_2O_3 and $NiFe_2O_4$ (points 1–2 in Fig. 9 d, and Supplementary Table s5). EDS mapping of $Ni_{30}Fe_{60}Cu_{10}$ alloy oxide cross-section revealed minimal fluoride presence (Fig. 9 e) compared to $Ni_{70}Fe_{20}Cu_{10}$ and $Ni_{50}Fe_{40}Cu_{10}$ alloys. After 24 h, the oxide scale on $Ni_{30}Fe_{60}Cu_{10}$ alloy remained limited to 169 ± 22 μm, with electrolyte penetration confined to small isolated pockets (in dark color, Fig. 9 d).

Despite the outstanding anode stability of the $Ni_{30}Fe_{60}Cu_{10}$ alloy, the aluminum produced had relatively high Fe contamination, resulting in a purity of 99.84 wt. % (Fig. 9 g). This contamination was likely attributed to the higher diffusion rate of Fe compared to Ni within the bulk alloy and to the increased fraction of the Fe_2O_3 phase in the scale [27]. Additionally, the high solubility of Fe_2O_3 in molten cryolite would inevitably increases Fe contamination in the produced aluminum [22]. Interestingly, a non-stoichiometric Fe-rich $Ni_xFe_{3-x}O_4$ spinel was formed at the oxide/alloy interface (point 3 in Fig. 9 d, and Supplementary Table s5), similar to that observed in the $Ni_{40}Fe_{50}Cu_{10}$ alloy. This conductive and stable spinel likely contributed to the low potential (about 4 V) observed in the $Ni_{30}Fe_{60}Cu_{10}$ alloy [35]. Furthermore, the high Fe content of alloy (60 wt. %) appeared to enhance the catalytic activity, as suggested by LSV results, where the anodic potential for $O_{2(g)}$ evolution increased by only 60 mV (from 2.96 V at j = 0.8 A·cm^{-2}) after 3 h of electrolysis (Supplementary Fig. s4). The calculated anode consumption rate for the $Ni_{30}Fe_{60}Cu_{10}$ alloy was 4 mm·year^{-1}.

3.7. *Influence of Ni/Fe ratio on mechanism of oxide scale growth*

We demonstrate the time dependent evolution of multilayered oxide scales on Ni–Fe-based OEAs, shedding light on its complex mechanisms. Understanding these mechanisms is essential for optimizing and developing alloys for metallic anode applications. The formation of the protective $NiFe_2O_4$ oxide on the Ni–Fe-based anode should involve defect-mediated diffusion of cations (Ni, Fe) and oxygen anions across the growing scale. The driving forces for these diffusion processes should arise from the chemical gradients of the cations (Ni/Fe ratio) within the alloy and from the activities of the anions (O^{2-}, F^-) established by coupled chemical and electrochemical reactions at the anode/electrolyte interface.

At the start of electrolysis, the pre-formed multi-oxide scale, generated ex-situ by high temperature air oxidation (Fig. 4), provides short-

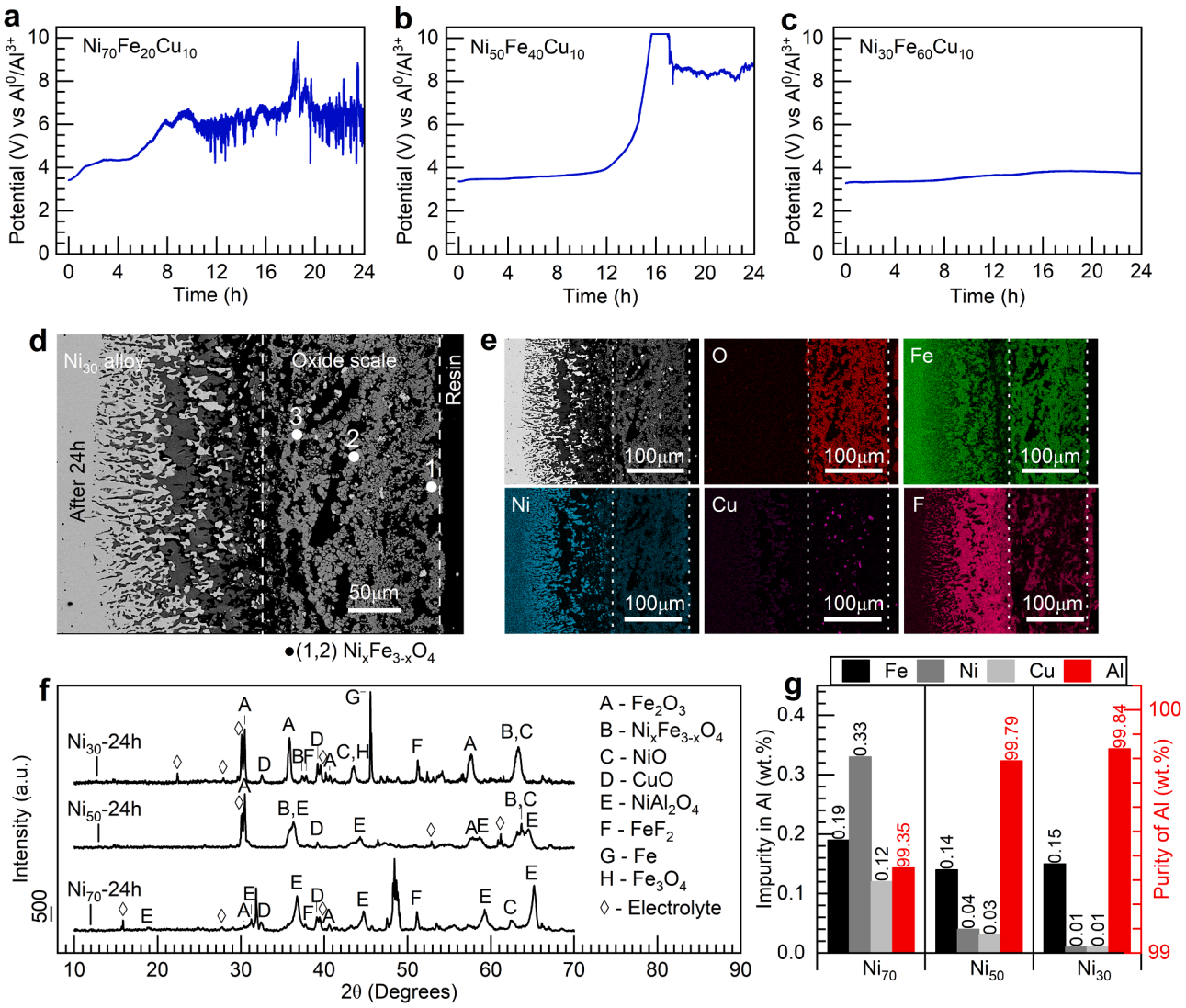

Fig. 9. Performance of $Ni_{70}Fe_{20}Cu_{10}$, $Ni_{50}Fe_{40}Cu_{10}$, and $Ni_{30}Fe_{60}Cu_{10}$ alloy, denoted as Ni_{70}, Ni_{50} and Ni_{30}, respectively, during electrolysis in molten fluoride bath at 800°C. (a, b, c) Evolution of anode potential as a function of electrolysis time. (d) SEM-BSE image of the anode cross-section after 24 h of electrolysis, with number markers (1,2,3) indicate the point at which EDS point analysis was performed (Supplementary Table s5). (e) EDS elemental mapping (O, Fe, Ni, Cu, and F) corresponding to SEM image (d). (f) XRD pattern of the oxide scale on the surface of the anode, and (g) aluminum purity with respect to anode alloy constituents after 24 h of electrolysis for Ni_{70}, Ni_{50} and Ni_{30} alloys.

term stability to the alloy [10,11,26]. Under continuous anodic polarization to evolve oxygen, the outermost oxide surface reaches a fully oxidized state, influenced by the high activity of oxygen at 800°C. Beneath this outer layer, NiO and Fe_2O_3 spontaneously react, forming $NiFe_2O_4$, which serves as a conductive and protective layer. Over prolonged operation, however, the phase ratio between NiO and Fe_2O_3—governed by the Ni/Fe ratio of the alloy—influences the sustained formation of $NiFe_2O_4$. This in-situ sustained growth of $NiFe_2O_4$ oxide under electrochemical oxidation conditions ultimately ensures the long-term stability of the anode alloy.

Based on the above results, Fig. 10 illustrates the mechanisms of unstable oxide scale growth in the high Ni alloy (Fig. 10 a) and stable oxide scale growth in the low Ni alloy (Fig. 10 b). In alloys with high Ni content 50–80 wt. %, a predominantly NiO layer forms, creating a diffusion barrier that slows outward diffusion of Fe, limiting the formation of $NiFe_2O_4$ within the scale (Fig. 4) [29,30]. Meanwhile, thermodynamically, NiO layer grows via internal oxidation of O^{2-} ions at the oxide/alloy interface—characterized as porous, thick scales with poor adhesion (Fig. 8 c, and Supplementary Fig. s1-c). Apparently, NiO scale on anode does not offer protection against molten fluorides species (F^-), due to its thermodynamic instability (Fig. 2). Under saturated bath conditions with high alumina activity, this NiO tends to convert to more stable $NiAl_2O_4$ (Fig. 8 d, and Supplementary Fig. s1-c), an insulating phase that raises the anode potential beyond the oxide dissociation potential limit. Once this potential is exceeded, the alloy consumption is accelerated through the formation of metallic fluorides such as NiF_2.

In contrast, alloys with lower Ni 30–40 wt. %, exhibit a dense and well-adherent Fe-rich oxide scale structure (Fig. 4 c, Fig. 7 a, and Fig. 9 d). The high Fe activity in the alloy and the larger volume fraction of Fe-oxide lead to the formation of a dual-layered structure: an outer $NiFe_2O_4$ layer at the oxide/electrolyte interface and an inner, non-stoichiometric Fe-rich $Ni_xFe_{3-x}O_4$ layer at the oxide/alloy interface (Fig. 7 c, Fig. 9 d). This inner layer, owing to its defect structure, enhances the conductivity of the scale [35]. With increased oxygen ion (O^{2-}) diffusion, this conductive non-stoichiometric layer eventually transforms into $NiFe_2O_4$, resulting in a dense and moderately thick oxide scale that limits further oxidation of base alloy. The outer $NiFe_2O_4$ layer sustains oxygen evolution while inhibiting electrolyte infiltration, and the inner layer restricts oxygen diffusion, continuously self-regenerating $NiFe_2O_4$ to supply the outer layer. This dual-layered structure slows the oxidation

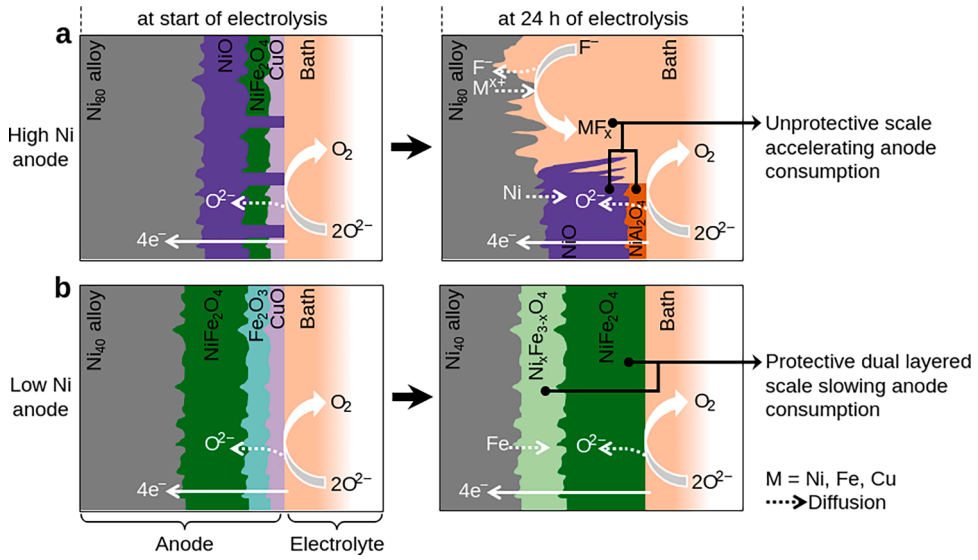

Fig. 10. Schematic illustration of the mechanism of oxide scale growth during electrolysis. (a) High Ni alloy $Ni_{80}Fe_{10}Cu_{10}$ forming an unprotective scale with a high consumption rate. (b) Low Ni alloy $Ni_{40}Fe_{50}Cu_{10}$ forming a protective scale with low consumption.

rate of the alloy, shifting it from a parabolic to a cubic regime (as seen in $Ni_{30}Fe_{60}Cu_{10}$ alloy in Fig. 3 a and Table 1) [32]. This promotes the growth of a stable, low consumption protective scale on OEA.

In summary, the Ni/Fe ratio of $Ni_{90-x}Fe_xCu_{10}$ alloys proves to be a critical factor influencing stability and performance of OEA. A decrease in the Ni/Fe ratio from 8 to 0.5 shows a positive impact on performance. Alloys with a Ni/Fe ratio between 8 and 1.25 are deemed unsuitable for OEA applications due to their high consumption rates, ranging from 5 to 16 mm·year^{-1}. In contrast, an optimal Ni/Fe ratio between 0.8 and 0.5 demonstrates the ability to form a protective and conductive oxide scale, with an anode consumption rate of less than or equal to 4 mm·year^{-1}.

4. Conclusions

This study demonstrates that Ni–Fe-based alloys hold significant promise as cost-effective, durable OEA materials for carbon-free aluminum production. We highlighted the essential role of thermodynamic analysis, oxidation kinetics, and long-hour electrolysis performance in fluoride melts for understanding the mechanisms of stable oxide scale growth and assessing alloy suitability.

A series of $Ni_{90-x}Fe_xCu_{10}$ alloys was successfully tested in low temperature KF-NaF-AlF_3-Al_2O_3 electrolytes at 800°C, achieving stable potential evolution and producing high purity aluminum. An optimized Ni/Fe ratio between 0.8 and 0.5 as in the $Ni_{40}Fe_{50}Cu_{10}$ alloy resulted in a stable and low anode potential, with metal purity approaching 99.9 wt. % after 24 h of electrolysis. This excellent anode performance is attributed to the formation of a kinetically slow-growing, self-regenerating $NiFe_2O_4$ oxide scale. This protective $NiFe_2O_4$ scale on the anode enhances corrosion resistance and maintains electrochemical stability.

Our findings underline the importance of long-hour electrolysis screening of OEA alloys for accurately evaluating their corrosion behavior and long-term viability. The optimized alloy composition identified in this study is key to achieving excellent anode performance. It will enable the design of a pilot-scale cell to accurately assess long-term durability in an industrially relevant setting, thereby advancing the goals of sustainable and carbon-free aluminum production.

CRediT authorship contribution statement

Kamaljeet Singh: Writing – original draft, Methodology, Investigation, Data curation, Conceptualization. **Thomas Luke Jamieson:** Writing – review & editing, Investigation, Data curation. **Gudmundur Gunnarsson:** Writing – review & editing, Validation, Supervision, Conceptualization. **Geir Martin Haarberg:** Writing – review & editing, Validation, Supervision, Conceptualization. **Isabella Gallino:** Writing – review & editing, Validation, Supervision, Conceptualization. **Ralf Busch:** Visualization, Supervision. **Jon Hjaltalin Magnusson:** Visualization, Project administration. **Gudrun Saevarsdottir:** Writing – review & editing, Validation, Supervision, Conceptualization.

Declaration of competing interest

The authors declare that they have no known competing financial interests or personal relationships that could have appeared to influence the work reported in this paper.

Acknowledgements

This manuscript is based on the Ph.D. thesis of Kamaljeet Singh, a double degree (cotutelle) doctoral thesis at Reykjavik University and the Norwegian University of Science and Technology (NTNU;2025:244). This work was financially supported by the Icelandic Research Fund (grant number 207242051), the German PROGRESS.NRW program, and additional funding from the Sustainability Institute and Forum 2024 at Reykjavik University. The authors are grateful to Trimet Aluminium Germany for providing ICP-OES analysis of the electrolyte samples.

Supplementary materials

Supplementary material associated with this article can be found, in the online version, at doi:10.1016/j.electacta.2026.148195.

Data availability

Data will be made available on request.

References

[1] Global Energy Transition A Roadmap to 2050, (n.d.). https://www.irena.org/publications/2018/Apr/Global-Energy-Transition-A-Roadmap-to-2050 (accessed October 29, 2024).
[2] G. Saevarsdottir, H. Kvande, B.J. Welch, Aluminum production in the times of climate change: the global challenge to reduce the carbon footprint and prevent carbon leakage, JOM 72 (2020), 1422–1422.
[3] A. Allanore, L. Yin, D.R. Sadoway, A new anode material for oxygen evolution in molten oxide electrolysis, Nature 497 (2013) 353–356.

[4] Y. Yan, D. Fray, Molten salt electrolysis for sustainable metals extraction and materials processing a review, Electrolysis: Theory Types Appl. (2010).
[5] Primary Aluminium Production - International Aluminium Institute, 2023 database, accessed on October 9, 2024, IAI, UK. (n.d.). https://international-aluminium.org/.
[6] D.R. Sadoway, Inert anodes for the Hall-Héroult cell: The ultimate materials challenge, JOM 53 (2001) 34–35.
[7] S.K. Padamata, K. Singh, G.M. Haarberg, G. Saevarsdottir, Review—primary production of aluminium with oxygen evolving anodes, J. Electrochem. Soc. 170 (2023) 073501.
[8] T.R. Beck, A non-consumable metal anode for production of aluminum with low-temperature fluoride melts, Essent. Read. Light Met.: Vol. 4 Electrode Technol. Alum. Prod. 4 (2016) 1104–1109.
[9] I. Gallino, M.E. Kassner, R. Busch, Oxidation and corrosion of highly alloyed Cu–Fe–Ni as inert anode material for aluminum electrowinning in as-cast and homogenized conditions, Corros. Sci. 63 (2012) 293–303.
[10] G. Gunnarsson, G. Óskarsdóttir, S. Frostason, J.H. Magnússon, Aluminum electrolysis with multiple vertical non-consumable electrodes in a low temperature electrolyte, Light Met. 2019 (2019) 803–810.
[11] K. Singh, G. Gunnarsson, J.H. Magnusson, G.M. Haarberg, G. Saevarsdottir, Performance evaluation of low-temperature KF-NaF-AlF3 electrolytes for aluminum electrolysis using vertical inert Cu–Ni–Fe alloy anodes, J. Electrochem. Soc. 170 (2023) 113507.
[12] D.R. Bradford, Inert Anode Life in Low Temperature Reduction Process, Northwest Aluminum Technologies, The Dalles, Oregon, 2005.
[13] A. Apisarov, A. Dedyukhin, O. Tkacheva, E. Nikolaeva, Y. Zaikov, P. Tinghaev, Physical-chemical properties of the KF-NAF-ALF3 molten system with low cryolite ratio, in: , 2009, pp. 401–403.
[14] A. Apisarov, A. Dedyukhin, E. Nikolaeva, P. Tinghaev, O. Tkacheva, Y. Zaikov, Liquidus temperatures of cryolite melts with low cryolite ratio, Metall. Mater. Trans. B 42 (2010) 236–242.
[15] I. Gallino, S. Curiotto, M. Baricco, M.E. Kassner, R. Busch, Homogenization of highly alloyed Cu-Fe-Ni: a phase diagram study, J. Phs. Eqil. Diff. 29 (2008) 131–135.
[16] J. Thonstad, P. Fellner, G.M. Haarberg, J. Hives, H. Kvande, A. Sterten, Aluminium Electrolysis: Fundamentals of the Hall-Héroult Process, Beuth Verlag GmbH, 2011.
[17] A. Solheim, Sodium in aluminium as a cell performance indicator: a quantitative framework, in: A.P. Ratvik (Ed.), Light Metals 2017, Springer International Publishing, Cham, 2017, pp. 633–639.
[18] H. Xiao, R. Hovland, S. Rolseth, J. Thonstad, Studies on the corrosion and the behavior of inert anodes in aluminum electrolysis, Met. Materi. Trans. B 27 (1996) 185–193.
[19] A. Roine, HSC Chemistry Software, Version 9.9.2.3, Metso Outotec, Pori, Finland, (2017). www.mogroup.com/hsc.
[20] A. Solheim, A. Sterten, Activity of alumina in the system NaF-AlF3-Al2O3 at NaF/AlF3 molar ratios ranging from 1.4 to 3, Light Met. 1999 (1999) 445–452.
[21] D.H. DeYoung, Solubilities of oxides for inert anodes in cryolite-based melts, in: A. Tomsett, J. Johnson (Eds.), Essential Readings in Light Metals: Volume 4 Electrode Technology for Aluminum Production, Springer International Publishing, Cham, 2016, pp. 1073–1081.
[22] O.-A. Lorentsen, Behaviour of nickel, iron and copper by application of inert anodes in aluminium production, PhD thesis, Norwegian University of Science and Technology, 2000.
[23] E. Gavrilova, G. Goupil, B. Davis, D. Guay, L. Roué, On the key role of Cu on the oxidation behavior of Cu–Ni–Fe based anodes for Al electrolysis, Corros. Sci. 101 (2015) 105–113.
[24] S. Helle, M. Pedron, B. Assouli, B. Davis, D. Guay, L. Roué, Structure and high-temperature oxidation behaviour of Cu–Ni–Fe alloys prepared by high-energy ball milling for application as inert anodes in aluminium electrolysis, Corros. Sci. 52 (2010) 3348–3355.
[25] D. Cao, Y. Ma, Z. Shi, J. Xu, X. Hu, Z. Wang, Corrosion behavior of Fe-Ni alloys in molten KF-AlF3-Al2O3 salts at 700 °C, Corros. Sci. 156 (2019) 32–43.
[26] V. Chapman, B.J. Welch, M. Skyllas-Kazacos, Anodic behaviour of oxidised Ni–Fe alloys in cryolite–alumina melts, Electrochim. Acta 56 (2011) 1227–1238.
[27] S.V. Divinski, F. Hisker, C. Herzig, R. Filipek, M. Danielewski, Self- and interdiffusion in ternary Cu-Fe-Ni alloys, Defect Diffus. Forum 237–240 (2005) 50–61.
[28] R. Haugsrud, T. Norby, P. Kofstad, High-temperature oxidation of Cu–30 wt.% Ni–15 wt.% Fe, Corros. Sci.. 43 (2001) 283–299.
[29] C.L. Muhich, V.J. Aston, R.M. Trottier, A.W. Weimer, C.B. Musgrave, First-principles analysis of cation diffusion in mixed metal ferrite spinels, Chem. Mater. 28 (2016) 214–226.
[30] J. Yu, K.M. Rosso, S.M. Bruemmer, Charge and ion transport in NiO and aspects of Ni oxidation from first principles, J. Phys. Chem. C 116 (2012) 1948–1954.
[31] L. Ying, C. Dengpeng, W. Wei, L. Dongsheng, W. Junwei, L. Yudong, S. Zhirong, Influences of heat treatment on the oxidation and corrosion behavior of Cu–Ni–Fe inert anodes for aluminium electrolysis, J. Alloys Compd. 832 (2020) 154848.
[32] T. Jamieson, D. Apel, A. Yasinskiy, R. Düssel, P. Decker, G. Gunnarsson, K. Singh, J. Magnusson, B. Adam, R. Busch, B. Friedrich, I. Gallino, On the long-term oxidation behaviour of homogeneous Ni–Fe–Cu alloys for CO2-free aluminium electrowinning applications at 800°C, J. Mater. Sci. (2025).
[33] R. Haugsrud, On the high-temperature oxidation of nickel, Corros. Sci. 45 (2003) 211–235.
[34] K. Singh, G.M. Haarberg, A.R. Mallah, G. Gunnarsson, T.L. Jamieson, I. Gallino, G. Saevarsdottir, Overpotential on oxygen-evolving platinum and Ni-Fe-Cu anode for low-temperature molten fluoride electrolytes, JOM 76 (2024) 3284–3293.
[35] S. Anjum, G.H. Jaffari, A.K. Rumaiz, M.S. Rafique, S.I. Shah, Role of vacancies in transport and magnetic properties of nickel ferrite thin films, J. Phys. D: Appl. Phys. 43 (2010) 265001.